Advanced Healthcare Materials

ADVANCED HEALTHCARE MATERIALS
www.advhealthmat.de

RESEARCH ARTICLE OPEN ACCESS

Deciphering the Role of Cancer Stem Cells in Breast Cancer Brain Colonization Using a Novel Patient-Derived Model

Stefania Faletti[1] | Cristina Richichi[1] | Daniela Osti[1] | Elena Ceccacci[1] | Giovanni Bertalot[1,2,3] | Camilla Cerutti[1] | Giuseppina Giardina[1] | Adriana Marinaro[1] | Brunella Costanza[1] | Valentina Gambino[1] | Elena Zaccheroni[1] | Daniela Tosoni[1,4] | Maria G. Filippone[1] | Marcello Del Corvo[1] | Yinxiu Zhan[1] | Teresa Gravina[5] | Davide Corà[5] | Monica Patanè[6] | Bianca Pollo[6] | Maria Giovanna Jodice[1,4] | Salvatore Pece[1,4] | Babette B. Weksler[7] | Ignacio A. Romero[8] | Pierre-Olivier Couraud[9] | Elisabetta Munzone[1] | Massimiliano Del Bene[10,11] | Francesco DiMeco[4,10] | Giuliana Pelicci[1,12]

[1]Department of Experimental Oncology, IRCCS, European Institute of Oncology (IEO), Milan, Italy | [2]Centre for Medical Sciences – CISMed, University of Trento, Trento, Italy | [3]Department of Anatomy and Pathological Histology, APSS, Santa Chiara Hospital, Trento, Italy | [4]Department of Oncology and Haemato-Oncology, University of Milan, Milan, Italy | [5]Department of Translational Medicine, Center for Translational Research on Autoimmune and Allergic Disease (CAAD), University of Piemonte Orientale, Novara, Italy | [6]Neuropathology Unit, Fondazione IRCCS Istituto Neurologico Carlo Besta, Milan, Italy | [7]Department of Medicine, Weill Medical College of Cornell University, New York, United States | [8]Department of Biological Sciences, The Open University, Milton Keynes, United Kingdom | [9]Institut Cochin, Centre National de la Recherche Scientifique UMR 8104, Institut National de la Santé et de la Recherche Médicale (INSERM) U567, Université René Descartes, Paris, France | [10]Department of Neurosurgery, Fondazione IRCCS Istituto Neurologico Carlo Besta, Milan, Italy | [11]Department of Pharmacological and Biomolecular Sciences, Università Degli Studi Di Milano, Milan, Italy | [12]Department of Translational Medicine, University of Piemonte Orientale, Novara, Italy

Correspondence: Giuliana Pelicci (giuliana.pelicci@ieo.it)

Received: 2 December 2025 | **Revised:** 25 February 2026 | **Accepted:** 1 March 2026

Keywords: brain metastasis | breast cancer | cancer stem cells | metastasis initiating cells | preclinical model

ABSTRACT

Brain metastases from breast cancer (BCBM) are fatal and lack effective treatments. Their cellular and molecular drivers remain poorly understood, partly due to limited preclinical models that fail to capture patient tumor heterogeneity. Cancer stem-like cells (CSCs) are implicated in metastatic dissemination; however, their specific role in brain metastasis remains unclear. In this study, CSCs are isolated from human BCBM specimens and characterized for stem-like properties, including CD44 and ALDH1 expression, sphere formation, tumorigenicity, and in vitro and in vivo self-renewal. Intra-nipple and intra-cardiac xenograft models demonstrate CSC ability to generate brain and bone metastases that recapitulate patient-specific dissemination patterns. Transcriptomic and functional analyses reveal cellular heterogeneity and identify a metastasis-initiating cell (MIC) subpopulation enriched in stemness and adhesion-related pathways. These MICs exhibit enhanced adhesion to brain endothelium and undergo brain-specific transcriptomic reprogramming that enables vascular co-option, resistance to stromal stress, and survival-promoting interactions with brain-resident cells. High-throughput drug screening indicates broad therapeutic resistance within the CSC compartment. Through the comprehensive characterization of BCBM-derived CSCs, this study establishes a clinically relevant model that identifies CSCs and the MIC subpopulation as key drivers of brain metastatic progression and as promising targets for the development of effective therapeutic strategies.

1 | Introduction

Brain metastases (BMs) are a life-threatening complication of solid tumors, occurring in 20–40% of adult cancer patients. Breast cancer (BC) is the second most frequent primary source, accounting for 15–25% of all BMs [1]. Among patients with metastatic breast cancer, 10–30% will develop BMs [2], with the highest risk observed in HER2-positive and triple-negative subtypes, which show a 2- to 5-fold greater incidence compared with luminal cancers [1].

Their occurrence has a detrimental impact on patient lifespan and quality of life, and their treatment remains an unmet clinical challenge [3]. Localized treatments such as surgical resection and radiation therapy are effective primarily in cases of oligometastatic disease. In contrast, widespread metastases require systemic therapies which have historically shown limited efficacy due to limited penetration across the blood–brain barrier (BBB) and uneven distribution within the central nervous system [4]. Recently, however, novel systemic agents such as the antibody–drug conjugate trastuzumab-deruxtecan and the HER2-selective tyrosine kinase inhibitor tucatinib have shown BBB penetration and achieve meaningful intracranial activity, marking a significant advance in the treatment of BCBMs [5, 6].achieve meaningful intracranial activity, marking a significant advance in the treatment of BCBMs [5, 6].

Despite the urgent need for improved therapeutic strategies for BCBMs, our understanding of the complex, multistep metastatic cascade to the brain remains limited. This challenge derives from the scarce availability of comprehensive BCBM models that are both experimentally feasible to handle and able to reflect the genomic heterogeneity of BM while accurately reproducing all the metastatic steps to the brain. Among the most used cellular models are 4T1 murine cells, MDA-MB-231, and $HER2^{+}$BT474 human cell lines. Although they have been deeply characterized, they fail to fully replicate the complexity of human BM [7]. Recent efforts have yielded only short-term BCBM primary cultures without achieving long-term stable in vitro models [8]. The brain tropism of most of these models has been established by selecting brain-seeking clones through serial xenotransplantation via direct brain injection or intracardiac (ICD) injection. While both these approaches are commonly used to study the later stages of metastatic processes, they bypass the critical early steps of the metastatic cascade, namely primary tumor growth, invasion, intravasation, survival in the bloodstream, adhesion, extravasation, and brain colonization [7]. Patient-derived xenografts (PDXs) developed by directly injecting human BM specimens into the murine mammary fat pads have had limited success. Of the many samples tested, only one was able to survive in vitro [9]. Thus, the establishment of fully characterized, long-term in vitro models that represent patient diversity is essential for advancing translational research focused on identifying specific BCBM vulnerabilities.

Single-cell analysis of patient-derived metastatic breast cancer cells revealed that metastases are hierarchically organized and sustained by a tumorigenic, multipotent subpopulation known as metastasis-initiating cells (MICs), which harbor stem-like features [10]. MICs initiate metastasis across various primary cancer types, and they have also been identified among circulating tumor cells [11–15].

In this study, we established patient BCBM-derived cancer stem cells (CSCs) in vitro cultures that closely recapitulate the gene expression and mutation profiles of the original human BM. These cells are tumorigenic and metastatic to the brain via different routes of injection, preferentially adhere to the brain endothelium, and are chemoresistant. Single-cell RNA-seq of BCBM-derived CSCs revealed high molecular heterogeneity and led to the identification of a specific MICs subset characterized by specialized molecular and phenotypic features, including stemness and adhesion signatures. Notably, MICs possess the ability to preferentially adhere to the brain endothelium, and the plasticity that enables them to home to both brain and bone niches. The identification of both bulk BCBM-derived CSCs and MICs highlights their critical role in the brain metastatic cascade and makes them clinically relevant models for studying BCBM.

2 | Methods

2.1 | Human BMs Processing and CSCs Culturing

BM samples were obtained with informed consent from BC patients (Table S1) and processed within 24 h of surgery. Tumors were dissociated into single cells, orthotopically injected into nude mice to generate a first PDX used as a source for CSC isolation, after which cells were cultured under conditions optimized for CSC growth [16]. Importantly, all BCBM-derived CSC cultures were exclusively established from tumors grown in PDX models, ensuring that CSCs were derived only after in vivo tumor propagation. Detailed protocols are provided in Supplementary Methods.

2.2 | CSCs Propagation and Self-renewal

For self-renewal, dissociated spheres were reseeded in MEBM with 50% methylcellulose (MethoCult SF, STEMCELL Technologies; 1,000–3,000 cells/35-mm dish). After two weeks, sphere-forming efficiency was calculated, and spheres were serially passaged. Detailed methods are described in Supplementary Methods.

2.3 | Flow Cytometry Analysis

To evaluate stem cell markers, integrins, and cell adhesion molecules expression, CSCs or cells derived from dissociated intra-nipple tumors were stained and analyzed by flow cytometry (FACS Vantage SE or BD FACS Celesta with HTS). At least 20,000 events were acquired per sample, and data were analyzed using FlowJo. Detailed staining panels and procedures are provided in Supplementary Methods.

2.4 | ALDEFLUOR Assay

The ALDEFLUOR kit (StemCell Technologies, Vancouver, Canada) was used to assess ALDH enzymatic activity in CSC cultures, according to the manufacturer's instructions, as detailed in Supplementary Methods.

2.5 | CSC Infection

Lentivirus packaging and transduction were carried out as described [17] and in Supplementary Methods.

2.6 | Animal Procedures

Mice were housed at the Cogentech animal facility accordingly to the guidelines set out in Commission Recommendation 2007/526/EC—June 18, 2007 on guidelines for the accommodation and care of animals used for experimental and other scientific purposes (i.e. housing under pathogen-free conditions at 22°C ± 2°C, 55% ± 10% relative humidity, and with 12 h d/light cycles; food and water provided ad libitum).

Orthotopic injections: female nu/nu CD1-nude (4–6 weeks old) mice were intraperitoneally anesthetized with tribromoethanol (0.1 mL/10 g of body weight). Spheres were dissociated, and 10^5 cells were resuspended in 2 µl of PBS and stereotaxically injected into the mice nucleus caudatus (coordinates from bregma: 1 mm posterior, 3 mm left lateral, 3.5 mm in depth) [17].

Intracardiac injections: female nu/nu CD1-nude (4–6 weeks old) mice were placed in dorsal recumbency under anesthesia with tribromoethanol (0.1 mL/10 g of body weight) intraperitoneally administered. Spheres were dissociated, and 4×10^5 cells were resuspended in 100 µl of PBS and delivered into the circulation through intracardiac injections using a 25-gauge insulin syringe.

Intra-nipple injections: female NOD scid gamma Il2-Rγ null (NSG) (6–8 weeks) were injected in the ninth mammary gland with 5×10^5 cells in 30 µL PBS:Matrigel (1:1) under isoflurane anesthesia. Tumor growth was monitored weekly, and mice were euthanized 4 weeks post-injection for tumor dissection. Details can be found in Supplementary Methods.

For all the described procedures, mice were monitored once a week to evaluate tumor progression by BLI, and those losing more than 20% of the body weight, exhibiting signs of morbidity, and/or development of neurological symptoms were sacrificed.

Brains and bones were harvested, formalin-fixed, and paraffin-embedded with Logos J Processor (Milestone Medical).

2.7 | Bioluminescence Imaging

BLI images of tumor-bearing mice were acquired using the PerkinElmer's IVIS Lumina Series III instrument 10 min after an intraperitoneal injection of D-luciferin (150 mg/kg) (Perkin–Elmer). Prior to imaging, the mice were anesthetized using gas anesthesia (3% isofluorane). At the time of sacrifice, brains and bones were collected and re-scanned ex vivo. The BLI signal intensities, measured as total flux (photons per second, [p/s]), were quantified using Living Image Software (Perkin–Elmer).

2.8 | Immunohistochemistry (IHC)

Human samples were fixed in Carnoy's solution, paraffin-embedded, and sectioned at 3 µm. For H&E, slides were stained in Carazzi hematoxylin solution, rinsed in running tap water, and counterstained in eosin solution.

Mouse tissues were formalin fixed and paraffin-embedded. 3 µm thick sections were cut and incubated overnight at 37°C before staining. H&E staining was performed with H&E Leica Kit Infinity for a full automated auto-stainer (Leica ST5020). Only lesions showing a solid and compact distribution of cancer cells were considered as metastases.

CSC spheres were suspended into 1% agarose, embedded in paraffin, and sectioned at 3 µm.

IHCs were performed according to standard procedures, as described in Supplementary Methods.

2.9 | Endothelial Cell Culture for Adhesion Assay

HUVECs (Lonza) were maintained in EGM2 on fibronectin-coated dishes (10 µg/mL) and used at passages 1–3. hCMEC/D3 cells were cultured in EBM2 supplemented with growth factors and 2.5% FBS on collagen-coated flasks to confluence (~1×10^5 cells/cm^2). All cells were grown at 37 °C, 5% CO_2. Detailed culture conditions are provided in the Supplementary Methods.

2.10 | PR60 Cell Labelling for Live-Imaging

1×10^6 PR60 cells were stained with 12.5 µM CellTracker Green CMFDA dye (Thermo Fisher Scientific) following the manufacturer's instructions, for 30 min at 37°C, 5% CO2 in serum-free DMEM medium (Euroclone). Cells were centrifuged at 300 × g for 5 min and resuspended in endothelial complete medium at 2×10^6 cells/ml for the flow-based adhesion assay.

2.11 | Flow-based Adhesion Assay

HUVECs or hCMEC/D3 cells were grown to confluence in Ibidi µ-Slides and subjected to flow-based adhesion of CMFDA-labelled PR60 cells under defined shear stress, as previously described [18, 19]. Interactions were recorded by time-lapse microscopy, and firm adhesion was quantified using ImageJ. Full assay details are provided in the Supplementary Methods.

2.12 | Whole Exome Sequencing Data Analysis

WES (whole exome sequencing) of CSCs, human BM, and PDX were performed with Illumina DRAGEN, filtered for xenograft contamination, annotated, and variants with VAF ≥0.05 and ≥10 supporting reads were retained (see Supplementary Methods).

2.13 | RNA Extraction—RT-qPCR

Total RNA was extracted from CSCs or frozen brain tissue using the Quick-RNA Miniprep Kit (Zymo Research) and reverse-transcribed to cDNA (High-Capacity cDNA Kit, Thermo Fisher). RT-qPCR was performed using SYBR Green or TaqMan probes

on a Viia7 system, and relative expression was calculated using the 2^-ΔΔCt method. Detailed protocols are provided in the Supplementary Methods.

2.14 | RNA Sequencing and Data Analysis

Total RNA was extracted as described. RNA integrity was checked on a Bioanalyzer 2000 (Agilent). 300ug of RNA was used in libraries preparation by using TruSeq Stranded Total RNAkit (Illumina) according to the manufacturer's instructions. Library quality was checked on a Bioanalyzer 2000 (Agilent). Libraries were multiplexed, clustered, and sequenced on an Illumina Novaseq 6000 by the IEO genomic unit.

Raw reads were mapped to the human reference genome hg19 using STAR [20]. Read quantification was calculated using the *featureCount* function of the Subread package [21]. *edgeR* was used to assess differential expression [22]. Differentially expressed genes (DEGs) were defined as those showing *FDR* ≤0.05 and linear fold-change ≥1.5. Pathway analysis and transcription factor prediction analysis were performed with QIAGEN's Ingenuity Pathway Analysis (IPA, QIAGEN Redwood City, www.qiagen.com/ingenuity). GSEA analysis was performed with the R package msigdbr and fgsea. GSEA-msigdb signature used in Figure 6A: TSUNODA_CISPLATIN_RESISTANCE_DN, MAHADEVAN_IMATINIB_RESISTANCE_DN, MARCHINI_TRABECTEDIN_RESISTANCE_DN, MASRI_RESISTANCE_TO_TAMOXIFEN_AND_AROMATASE_INHIBITORS_DN.

2.15 | Single-cell RNA Sequencing

Single-cell RNA-seq was performed on PR60 "Input" cells from IN-derived tumors and "Adhered" cells isolated after flow-based adhesion to hCMEC/D3 monolayers. Cells were processed using the 10x Genomics Chromium Single-Cell 3' kit, and libraries were sequenced on an Illumina NovaSeq 6000. Data were quality-controlled, normalized, and analyzed using Seurat, including dimensionality reduction, clustering, and gene signature scoring. Detailed procedures, including adhesion/stemness/differentiation of gene signatures, differential expression, and gene ontology analyses, are provided in the Supplementary Methods.

2.16 | Drug Screening

CSCs were screened with a 295-compound bioactive library, assembled from commercial collections (Lopac 1280, Selleck Epigenetics, MicoSource 2010; Table S3) using Tecan Freedom EVO and CellTiter-Glo 3D assays. Primary hits were validated in dose–response assays (0.25–2.5 μM), and inhibition and assay quality (Z'-factor) (Figure S3) were calculated as described [23, 24] and in Supplementary Methods.

2.17 | IC50 Determination

For the measure of the half maximal inhibitory concentration (IC50) value, CSCs were seeded in 96-well black clear flat (Greiner) plates at 9000 cells/well. Concentrations ranging from 20 μM to 0,6 nM for Abemaciclib, and from 10 μM to 1 nM for Cisplatin, Palbociclib, and Imatinib were tested. 3 days after treatment, cell viability was assessed through CellTiter-Glo 3D.

2.18 | Statistical Analysis

All statistical analyses were performed using GraphPad Prism version 10.4.1 (RRID: SCR_002798). Data were presented as mean ± SD. Comparisons between two groups were performed using an unpaired Student's *t*-test, while ANOVA followed by Tukey's post hoc test was used for multiple group comparison. To evaluate the in vivo tumorigenicity of BM-derived CSCs, Kaplan–Meier survival analysis was performed.

3 | Results

3.1 | Breast Cancer Brain Metastases Harbor Cancer Stem Cells for In vitro Modeling

To assess the presence of CSCs within human BCBM, we generated intracranial PDXs from 24 clinically and molecularly heterogeneous BCBM specimens (Table S1). Tumor cells were implanted into the brain of immunocompromised CD1 nude mice, resulting in successful tumor formation in 14 cases. Xenograft tumors were dissociated into single-cell suspensions and cultured under defined serum-free conditions optimized for CSC enrichment [16]. We established cultures from 7 out of 14 PDXs. The complete model-development pipeline, linking each model to subsequent analyses, is summarized in Figure 1A. Among the established CSC cultures, we selected the most easily expandable models for detailed characterization, focusing on three CSC samples, namely PR60, FA40, and FR57-II, which were derived from BCBMs of distinct molecular subtypes (i.e., Luminal B for PR60 and HER2-positive for both FA40 and FR57-II). These cells grew as non-adherent tumorspheres (Figure 1B), a known hallmark of CSC-enriched across multiple tumor types [25–28]. Confirming the stemness of these cultures, BCBM-derived CSCs displayed a wide expression of the putative breast cancer stem cell markers CD24 (PR60: 92.4%; FA40: 96.6%; FR57-II 96.9%; LD1972: 0.16%; MMR73: 36%), CD44 (PR60: 71.1%; FA40: 99.9%; FR57-II: 21%; LD1972: 55.2%; MMR73: 41.8%), and aldehyde dehydrogenase (ALDH1: PR60: 15.4%; FA40: 29.6; FR57-II: 2.7%; LD1972: 8.2%; MMR73: 19%) (Figure 1C; Figure S1A, B). Functionally, CSCs are defined by their capacity for self-renewal. Therefore, we tested the capacity of BCBM-derived CSCs to form spheres and their consistency over serial plating. The efficiency of sphere formation varied among different BCBM-derived CSC samples, and was conserved both through serial plating (PR60 first plating: 11.8 ± 1.92%, second plating: 10.7 ± 2.11%, third plating: 9.8 ± 1.26%; FA40 first plating: 8.9 ± 1.13%, second plating: 8.8 ± 1.04; FR57-I first plating: 1.8 ± 0.44%, second plating: 1.7 ± 0.37%; FR57-II first plating: 2.1 ± 0.33%, second plating 2.0 ± 0.19%; LD1972 first plating: 17.73 ± 2.9%, second plating 20.25 ± 3.18%; MMR73 first plating: 14.7 ± 0.36%, second plating 11.63 ± 3.29%; CA56 first plating: 2.10 ± 0.68% (Figure 1D; Figure S1C), and across several passages (Figure 1E). This consistency also supported the CSCs long-term growth (Figure 1F). The isolated BCBM-derived CSCs retained the molecular profile of their BM of origin in terms of the expression of key BC diagnostic markers: estrogen receptor (ER), progesterone receptor (PgR), and human epidermal growth factor

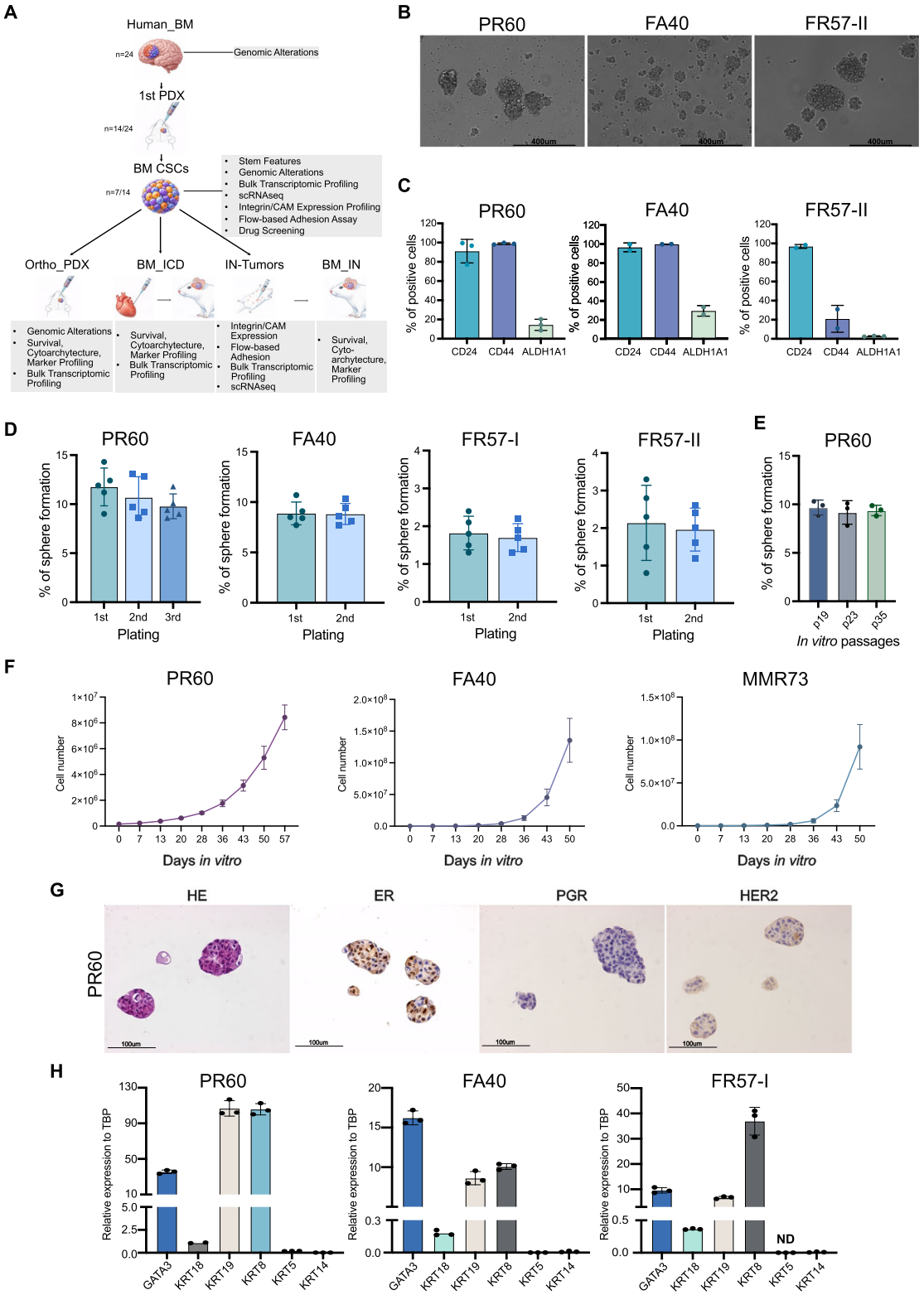

FIGURE 1 | CSCs can be isolated from BMs and cultured in vitro. (A) Schematic representation of the experimental pipeline from BM patient samples to CSC model generation and downstream analyses. (B) Representative image of PR60, FA40, and FR57-II CSCs grown as floating spheres. Scale bars: 400 μm. (C) Quantification of the breast cancer stem cell markers (CD24, CD44, and ALDH1) in the indicated CSC cultures by flow cytometry analysis (CD24: $n = 5$ PR60; $n = 2$ FA40; $n = 2$ FR57-II; CD44: $n = 4$ PR60; $n = 2$ FA40; $n = 2$ FR57-II; ALDH1: $n = 4$ PR60; $n = 2$ FA40; $n = 3$ FR57-II, mean ± SD). (D) Sphere formation ability of the indicated CSC cultures upon the indicated serial plating ($n = 5$, mean ± SD). (E) Stability of sphere formation ability in the representative PR60 CSC assessed at different passages ($n = 3$, mean ± SD). (F) CSC growth assessed by the 3T3 growth curve assay. Cell number was determined by manual counting ($n = 3$, mean ± SD). (G) Immunohistochemistry in sphere sections from PR60 CSC cultures for ER, PgR, and HER2. Scale bars: 100 μm. (H) Expression of epithelial markers (GATA3, KRT18, KRT19, KRT5, KRT8, KRT14) in the indicated CSC cultures measured by RT-qPCR ($n = 3$, mean ± SD). TBP (TATA-box Binding Protein) was used as the housekeeping gene for normalization.

receptor 2 (HER2). Specifically, PR60 CSCs were ER-positive but negative for HER2 and PgR, consistent with a Luminal B subtype. CA56 CSCs exhibit an ER-positive, PgR-negative, and HER2-positive profile, supporting their classification as Luminal B/HER2-positive subtype. MMR73 CSCs exhibit an ER-positive, PgR-negative, and HER2-positive profile, supporting their classification as the HER2-positive subtype, as the corresponding human BM (Figure 1G; Figure S1D, E, and Table S1).

Similar to BCBM which retain their epithelial identity even in the brain microenvironment [29], CSCs also retained the expression of epithelial markers (Figure 1H; Figure S1E, F), while showing very low expression level of the neural-related markers Glial Fibrillary Acidic Protein (GFAP), Tubulin Beta 3 (TUBB3), and Nestin (NES) (Figure S1G), which are typically associated with primitive brain tumors (Figure S1H). Only the SOX2 gene was barely expressed across samples (Figure S1C), aligning with its role in BCBM [30].

Hence, we managed to isolate and culture BCBM-derived CSCs endowed with stem-like properties and retaining their epithelial identity, all features that support their potential as valuable human BCBM preclinical models.

3.2 | Intracranial Xenografts from BCBM-derived CSCs Recapitulate the Parental BM

Three representative BCBM-derived CSC samples (PR60, FA40, and FR57-II) were selected for orthotopic xenograft modeling based on their distinct patient and tumor characteristics, including breast cancer subtypes and treatment histories (Table S1) and their in vitro CSC properties (Figure 1). Tumors developed in 100% of the injected animals (Figure 2A; Figure S2A) recapitulating the patient tumor cytoarchitecture (hematoxylin-eosin [H&E] staining) and molecular phenotype, including the expression of the epithelial (Gata3 and PanCK) and diagnostic markers (ER, PgR, HER2) (Figure 2B; Figure S2B) and the lack of neuronal markers (GFAP, Nestim, Sox2) (Figure S2C).

Among the tested samples, we focused on PR60 CSCs given their shorter latency (Figure 2A). PR60-driven PDXs preserved the majority of the mutations found in the PR60 CSCs, and both CSCs and PDXs mirrored the mutational landscape of the human BM (Figure 2C; Table S2). Moreover, their tumorigenicity was maintained upon serial intracranial injections, either in terms of mice survival (Figure 2D) and tumor incidence in limiting dilution conditions (Figure 2E). Also, the expression of stemness (Figure 2F) and epithelial (Figure 2G) markers was maintained upon serial engraftment, as well as the lack of neural marker expression (Figure S2D). Overall, these data support BCBM-derived CSCs ability to generate xenotumors that retain the patient-specific molecular and histological traits of their parental BM.

3.3 | PR60 CSCs Recapitulate the Patient Metastatic Clinical Course In vivo

To assess the metastatic potential and organotropism of BCBM-derived CSCs, luciferase-expressing PR60 CSCs were ICD-injected in nude mice, a procedure that mimics cancer cell dissemination through the bloodstream and subsequent implantation in secondary organs [31]. Mice were monitored for the appearance of symptoms suggestive of brain malignancies, and tumor formation was further monitored through in vivo bioluminescence imaging (BLI). The mean survival of transplanted mice was 77 ± 23 days, a time at which BLI confirmed the tumor burden (Figure 3A). Histological analysis (H&E staining) further revealed that PR60 CSCs formed tumors of various sizes in different cerebral locations (Figure 3B). Multifocal brain lesions were observed in 82% of injected mice (Figure 3C), all of which exhibited macrometastases; notably, 18% of all injected mice harbored both macrometastases and additional micrometastases (Figure 3D).

We then transplanted luciferase-positive PR60 CSCs by intra-nipple (IN) injection, a procedure that recapitulates the whole metastatic process [32]. Primary tumors developed in 100% of mice (Figure 3E) and were surgically removed after 30 days, allowing metastases to progress in the absence of the primary tumor, mimicking a clinical scenario. The mean survival of BM-bearing mice was 78 ± 23 days. Brain tumor burden was monitored through BLI (Figure 3F) and confirmed through H&E staining (Figure 3G). Metastatic tumors developed in 50% of the animals: multi-focal lesions were observed in the brain of 37.5% of the mice, while 12.5% of the animals reported a single BM (Figure 3H). Among the mice that developed tumors, all exhibited brain macrometastasis, and 25% of all injected mice displayed both macrometastases and micrometastases (Figure 3I).

BMs formed upon either ICD or IN injection were similar basing on their cytoarchitecture and expression of epithelial (Figure 3J) and neural (Figure S3A) markers, and both closely resembled the human BM of origin (Figure 2B; Figure S2C). Moreover, they preserved the receptor status of the corresponding patient-derived BM, showing strong ER positivity (90% of tumor cells), absence of PgR expression, and HER2 positivity (IHC score 1+), consistent with classification as Luminal B–like breast cancer brain metastases (Figure 3K).

We observed a high incidence of bone metastasis following both ICD (Figure S3B, C) and IN (Figure S3D) injections. Following ICD injection, 82% of the injected mice developed a single brain lesion, whereas 18% presented with multifocal lesions (Figure S3E). Notably, all detected tumors were macrometastases, with no micrometastases observed at the time of sacrifice (Figure S3F).

Regarding IN injection, the frequency of single and multiple bone lesions was identical at the time of animal sacrifice (Figure S3G). 71% of all injected mice exhibited bone macrometastasis, and 14% of them both macro and micrometastasis (Figure S3H). The cytoarchitectural features of bone lesions resulting from both ICD (Figure S3I) and IN (Figure S3J) injections were consistent with PR60-driven origins.

Overall, these data clearly demonstrate that PR60 CSCs can metastasize both directly via the bloodstream and through primary tumor progression with a metastatic pattern that closely mirrors the PR60 patient's clinical progression.

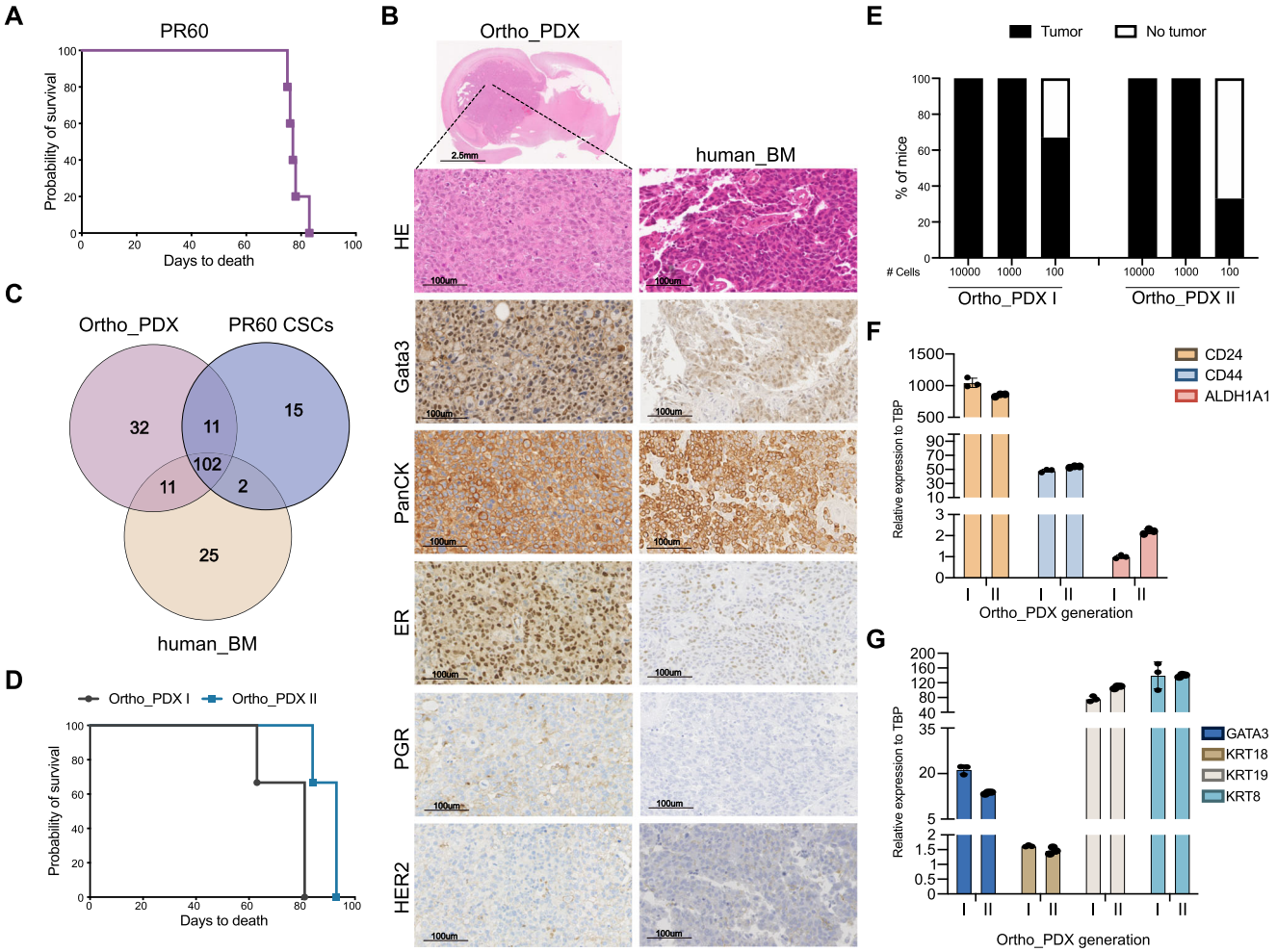

FIGURE 2 | CSCs-derived intracranial tumors resemble the original BM. (A) Kaplan-Meier curve showing probability of survival in mice bearing intracranial tumors derived from PR60 CSCs injection ($n = 5$). The X-axis indicates days post-tumor implantation. (B) Hematoxylin and Eosin (H&E) staining and immunohistochemistry for Gata3, PanCK, ER, PgR, and HER2 on sections of intracranial xenografts derived from PR60 CSCs injection (Ortho-PDXs) and the corresponding human specimen (human_BM). Panel include a low-magnification overview (scale bars: 2.5 μm) and higher-magnification images (scale bars: 100 μm). (C) The number of genomic alterations common among i) PR60 CSCs, defined as cancer stem cells (CSCs) isolated from the initial patient-derived xenograft (PDX) generated from the corresponding human BM, ii) the original human brain metastasis of the patient from which they have been isolated (human_BM), and iii) the corresponding tumor arose upon orthotopic injection of CSCs into mice brain (Ortho_PDX). (D) Kaplan-Meier survival curves of mice serially transplanted with PR60 CSCs. Tumors harvested from primary xenografts (first generation, Ortho_PDX I) were used to establish secondary PR60 CSC cultures, which were then intracranially transplanted into a second cohort of mice (second generation, Ortho_PDX II) ($n = 3$ mice per group). The X-axis indicates days post-tumor implantation. (E) Tumor incidence in mice intracranially injected with serial concentrations of first-generation (Ortho_PDX I) or second-generation (Ortho_PDX II) PR60 CSCs, as described in (D). (F), (G) Expression of stem cell markers (CD24, CD44, ALDH1) (F) and the epithelial markers (GATA3, KRT18, KRT19, KRT8) (G) in the indicated first (Ortho_PDX I) or second generation (Ortho_PDX II) intracranial xenografts derived from PR60 CSCs measured by RT-qPCR ($n = 3$, mean ± SD). TBP (TATA-box Binding Protein) was used as the housekeeping gene for normalization.

3.4 | Metastatic Xenotumors Display Organ-specific Transcriptomic Reprogramming

Having assessed that PR60 CSCs are able to seed BMs recapitulating the human BM of origin, we sought to further explore their molecular traits. Both PR60 CSCs (Figure 4A) and the tumors formed upon their orthotopic transplantation (PR60-Ortho-PDX) (Figure 4B) revealed a strong transcriptional correlation with those of the human BM. Further, when IN-injected, PR60 CSCs reproducibly formed tumors (PR60-IN) whose gene expression profiles resembled those of the patient's primary breast tumor (human_PB) (Figure 4C). In support of this, the murine and human breast lesions are morphologically and immunophenotypically comparable. (Figure S1A).

Bone tumors formed upon intracardiac injection (PR60-bone-ICD) clustered separately from both intracranial tumors (PR60-Ortho-PDX and PR60-brain-ICD) and IN tumors (Figure S1B). Furthermore, the gene expression profiles of all brain tumors (PR60-Ortho-PDX and PR60-brain-ICD) were highly correlated with each other but showed lower correlation with bone tumors (PR60-bone-ICD), indicating that PR60 CSCs undergo organ-specific transcriptomic rewiring during colonization (Figure 4D). Of note, these results were consistently observed across four

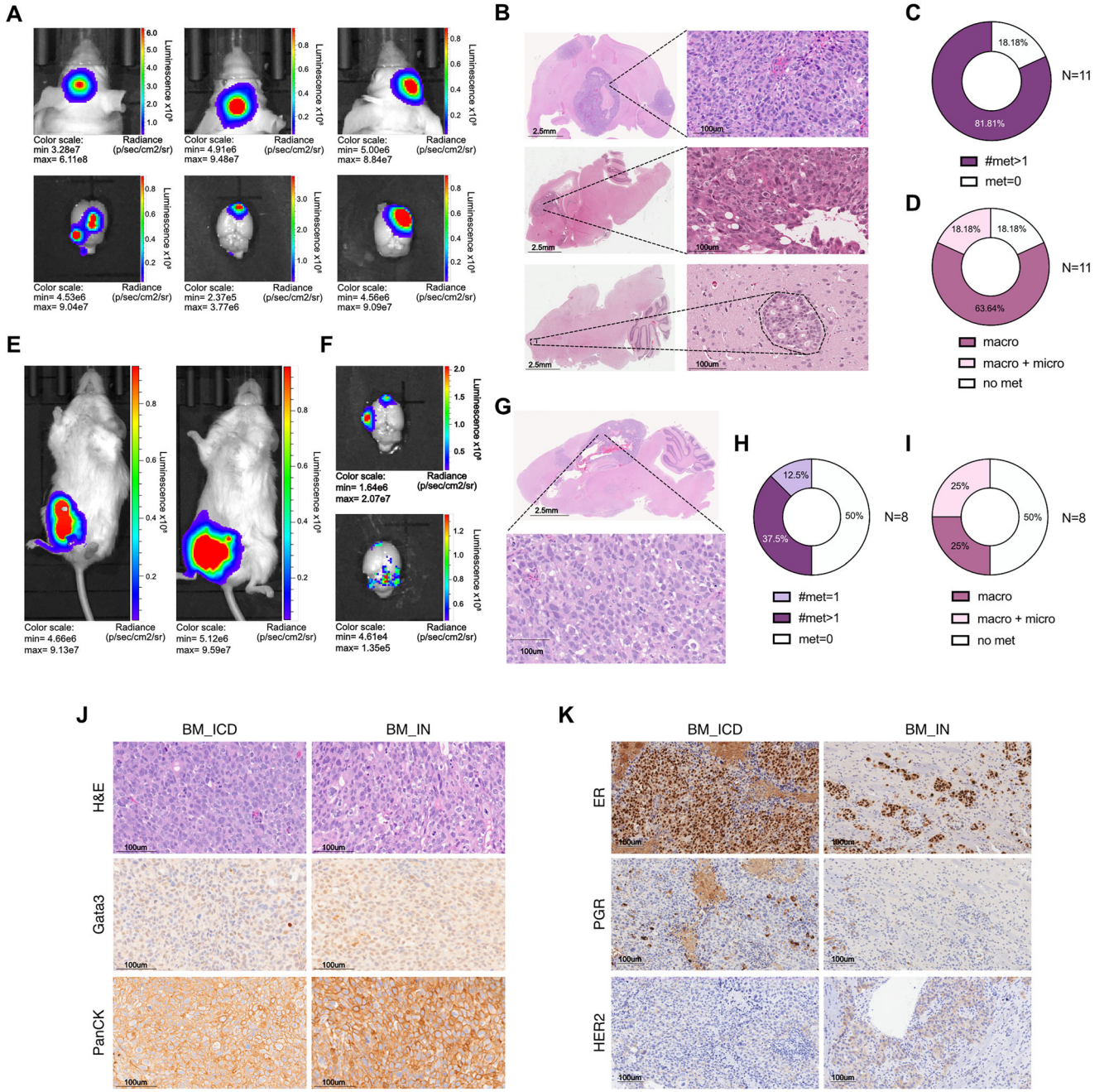

FIGURE 3 | PR60 CSCs recapitulate the metastatic clinical course of the patient. (A) Bioluminescence images of BMs derived from luciferase-expressing PR60 CSCs following intracardiac injection. Ex vivo bioluminescent imaging of isolated brains is shown below. (B) Representative Hematoxylin and Eosin (H&E) staining of BMs as in (A). Panel includes low-magnification overviews (scale bars: 2.5 μm) and higher-magnification images (scale bars: 100 μm). (C), (D) Pie charts for metastatic distribution (no metastasis, multifocal metastasis) (C) and metastatic outcomes (macrometastasis, macrometastasis and micrometastasis, no metastasis) (D) upon intra-cardiac injection (n = 11 mice). (E), (F) Bioluminescence images of primary tumors (E) and BMs in isolated brains (F) following intra-nipple injection of luciferase-expressing PR60 CSCs. (G) Representative Hematoxylin and Eosin (H&E) staining of a BM derived from luciferase-expressing PR60 CSCs following intra-nipple injection. Shown are a low-magnification (scale bars: 2.5 μm) and a higher-magnification image (scale bars: 100 μm). (H), (I) Pie charts for metastatic distribution (no metastasis, single metastasis, and multifocal metastasis) (H) and metastatic outcomes (macrometastasis, macrometastasis and micrometastasis, no metastasis) (I) upon intra-nipple injection. (J), (K) Hematoxylin and Eosin (H&E) staining and immunohistochemistry for the epithelial markers Gata3 and PanCK (J), and for the diagnostic tumor markers ER, PgR, and HER2 (K) on BMs derived from PR60 CSCs following intra-cardiac (BM_ICD) or intra-nipple injection (BM_IN). Scale bars: 100 μm.

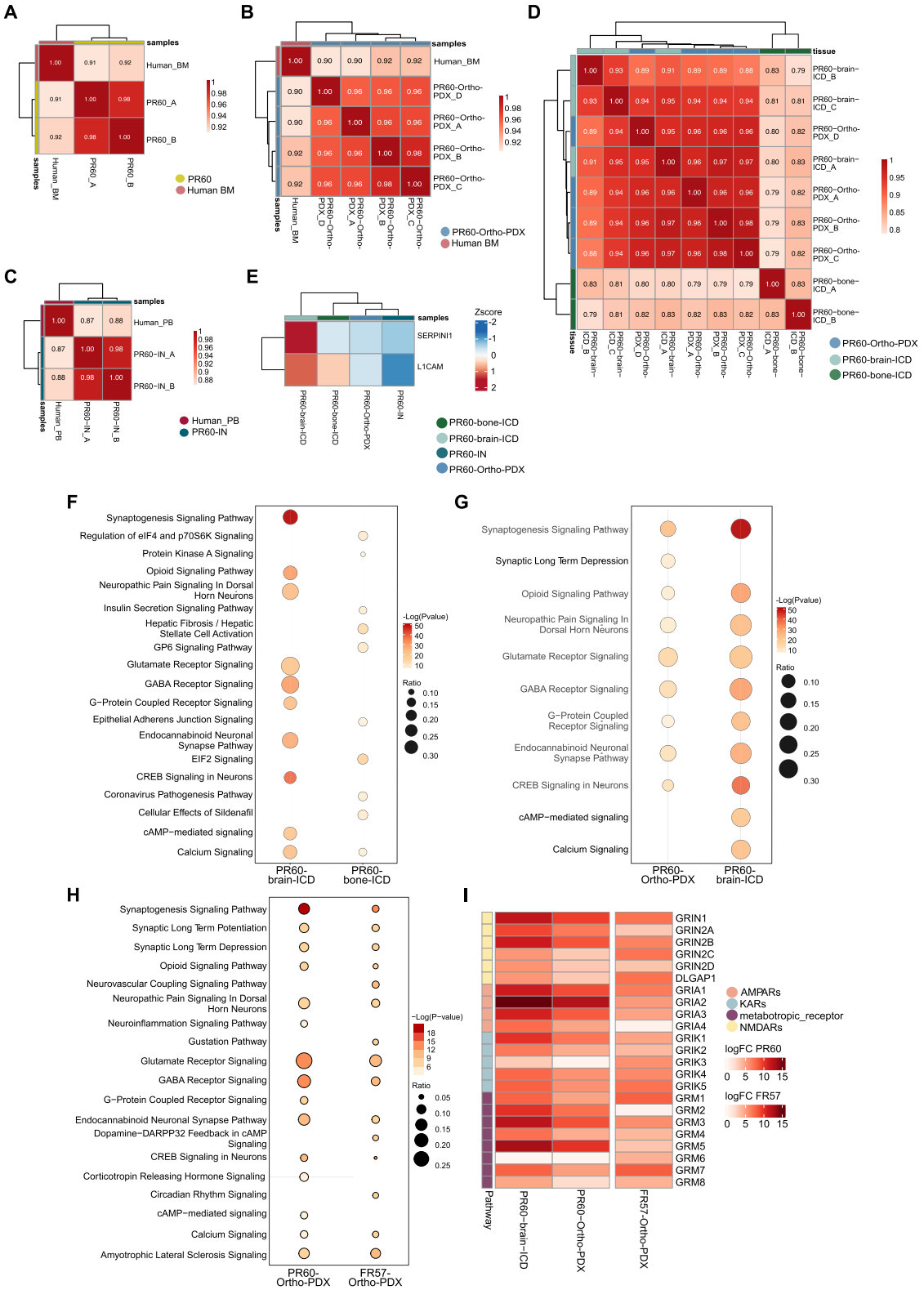

FIGURE 4 | Transcriptomic profiles of metastatic xenotumors are shaped by organ-specific niches. (A–D) Heatmaps showing the correlations among the expression profiles of PR60 CSCs (PR60_A and PR60_B) and the corresponding human BM (Human_BM) (A), intracranial tumors (PR60_Ortho_PDX_A, PR60_Ortho_PDX_B, PR60_Ortho_PDX_C, PR60_Ortho_PDX_D) and the human BM (Human_BM) (B), orthotopic intra-nipple tumors (PR60-IN_A, PR60-IN_B) and the human primitive breast (Human_PB) (C), intracranial tumors (PR60_Ortho_PDX_A, PR60_Ortho_PDX_B, PR60_Ortho_PDX_C, PR60_Ortho_PDX_D), brain (PR60_brain_ICD_A, PR60_brain_ICD_B, PR60_brain_ICD_C) and bone (PR60_bone_ICD_A, PR60_bone_ICD_B) metastases derived from PR60 CSCs upon intracardiac injection (D). Red represents positive correlations, with darker shades reflecting stronger correlations. The numerical values within the tiles represent the correlation coefficients between the indicated samples. (E) Heatmap showing the Z-score of expression of L1CAM and SERPINI1 genes in orthotopic (PR60-Ortho-PDX and PR60-IN) and metastatic tumors (PR60-brain-

different mice, demonstrating the robustness and reproducibility of the in vivo PR60 CSC model.

After extravasation, PR60 CSCs must survive in the hostile brain microenvironment. Key to this early survival is vascular co-option [33]. Metastatic tumors (PR60-brain-ICD and PR60-bone-ICD) exhibited upregulated expression of L1CAM, a mediator of vascular co-option, compared to orthotopic tumors (PR60-Ortho-PDX and PR60-IN) (Figure 4E). Additionally, these metastatic tumors increased Serpin1 expression, a factor that shields tumor cells from plasmin-mediated suppression by reactive brain stroma, supporting metastatic outgrowth [34] (Figure 4E).

To further dissect molecular adaptation, we compared the gene expression profile of PR60-brain-ICD and PR60-bone-ICD tumors with that of in vitro cultured PR60 CSCs. Brain tumors showed a distinct enrichment of neuronal-related pathways, including synaptogenesis and glutamate receptor signaling, that were absent in bone tumors (Figure 4F). Strikingly, this transcriptomic rewiring was confirmed in tumors from orthotopic injections of both PR60 (Figure 4G) and FR57 CSCs (Figure 4H), highlighting how the brain microenvironment shapes BCBM-derived CSC gene expression. In this regard, we reported the enrichment of Synaptogenesis Signaling Pathway and Glutamate Receptor Signaling (Figure 4F–H), as well as the increased expression of glutamatergic receptors (NMDA, AMPA, Kainate, and Metabotropic Receptors) across all brain tumors, likely mediating active synaptic-like communication between neurons and tumor cells within the brain microenvironment (Figure 4I). Notably, these mechanisms are recognized as critical for metastatic colonization [35].

3.5 | Shear-resistant Adherent PR60 CSCs Retain Organotropism to the Brain and Harbor Metastasis-Initiating and Stem-Cell Features

A key early step in the metastatisation process to the secondary organ, it is the ability of tumor cells to adhere and transmigrate to and across the vasculature, formed by endothelial cells (ECs). ECs from different regional vascular beds exhibit distinct specific molecular composition, which results in distinct tumor cell adhesion to ECs. In particular, the BBB composition and structure possess unique features among the vasculature system, and brain endothelial cells express a unique molecular signature [4]. By investigating the membrane associated adhesome of PR60 CSCs, we found that these cells displayed expression of active-form integrins and membrane-associated cell adhesion molecules (Figure 5A, B), including CD44, integrin $\alpha4\beta1$ (CD49d/CD29), VCAM-1 (CD106), and MUC1 (CD227), all of which are known mediators of breast cancer cell adhesion to the BBB [36]. Notably, CD227 and CD155 are also associated with increased invasiveness and poor prognosis in breast cancer [37, 38]. Importantly, molecularly diverse CSCs (FA40 and FR57-II) showed a similar pattern of expression of adhesive molecules (Figure S2A–C). Moreover, PR60 CSCs exhibited shear-stress resistance, a key feature for survival in circulation and metastatic progression, demonstrating enhanced firm adhesion to human brain endothelial cells (hCMEC/D3) compared to control endothelial cells (HUVECs) under real-time flow conditions (Figure 5C, D). Interestingly, by exploiting the IN injection model, which mimics natural breast cancer location and progression, we found that freshly isolated cells from PR60 IN-injected PDXs retained the same adhesive and organotropic features observed in vitro. Indeed, these cells similarly expressed the membrane-associated adhesome (Figure 5A, B), resisted shear-stress conditions (Figure S2D), and displayed preferential adhesion to brain endothelial hCMEC/D3cells over HUVECs (Figure 5E). Supplementary movie files illustrate this in greater detail (Additional Files Movies S1 and S2).

Based on these findings, we characterized the molecular features of the PR60 cell subset derived from freshly dissociated IN tumors that adhered to hCMEC/D3 cells using single-cell RNA sequencing (scRNAseq). We analyzed both the adherent fraction (Adhered) and the entire PR60 CSC population (Input). After quality control, 4,180 Adhered cells and 8,486 Input cells were retained and integrated, resulting in 12 different clusters (Figure 5F). While most of the clusters were evenly populated by cells from both the Adhered and Input groups, clusters 2 and 7 were depleted by adhered cells (Figure 5G). To further explore the transcriptional signature of the adhered PR60 cells to brain ECs, we examined the expression of a selected set of adhesion-related genes. Cluster 2 and 7 had lower expression of these genes, while cluster 4, 11, and subpopulations of clusters 0 and 5 showed higher expression of adhesion-related genes (Figure 5H), particularly those associated with integrin-mediated cell adhesion (Figure 5I). Interestingly, the distribution of stem-related genes (Figure 5J) closely mirrored that of adhesion-related genes (Figure 5H) and was inversely associated with differentiation gene expression (Figure 5K). Notably, the subpopulation characterized by the $CD44^{high}/CD24^{low}$ phenotype, which defines highly tumorigenic breast cancer stem cells with metastatic potential and therapy resistance [39], was mainly distributed in cluster 4 and 11 (Figure 5L), endowed with the higher expression of adhesion- and stem-related genes. Cluster 4 and 11 were also enriched with gene signatures associated with metastatic breast tumors (Figure 5M), thus linking stemness features, adhesive properties, and metastatic potential. Gene ontology analysis further revealed that genes enriched in clusters with high adhesion gene expression (clusters 0, 4, 5, and 11; Figure S2E) were involved in focal adhesion, epithelial to mesenchymal transition, and transforming growth factor beta (TGF-β) signaling pathways, key processes

ICD and PR60-bone-ICD). (F–H) Bubble plots showing the top enriched KEGG pathways identified by RNA sequencing analysis comparing brain (PR60_brain_ICD) and bone (PR60_bone_ICD) metastases from intracardiac injection of PR60 CSCs (F), intracranial tumors (PR60_Ortho_PDX) and brain metastases (PR60_brain_ICD) from intracardiac injection of PR60 CSCs (G), and orthotopic tumors derived from PR60 (PR60_Ortho_PDX) and FR57 (FR57_Ortho_PDX) CSCs (H). All tumor groups were compared to the corresponding patient-derived CSC sample. Bubble size indicates the ratio of enriched pathways (Ratio), while color intensity represents the significance of the enrichment (−logPvalue). (I) Heatmap showing the expression of glutamatergic receptors (AMPA [AMPARs], Kainate receptor [KARs], NMDA [NMDARs], and metabotropic receptors) in the indicated samples. A gradient of light red to dark red indicates low to high expression levels in the heatmap.

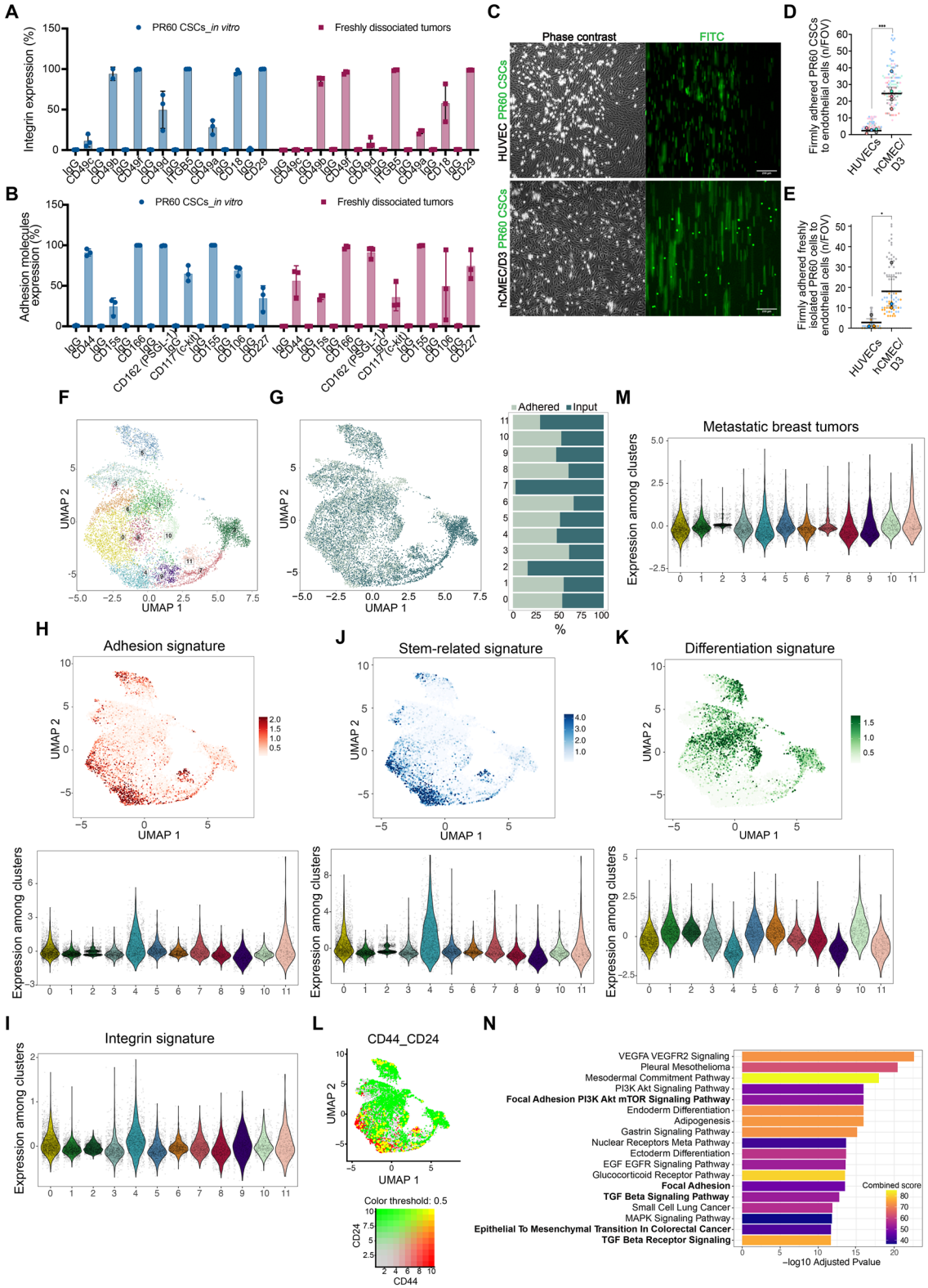

FIGURE 5 | Shear-resistant adherent PR60 CSCs retain organotropism to the brain and harbor metastasis-initiating and stem-cell features. Expression of (A) integrins and (B) cell adhesion molecules on PR60 CSC surface flow cytometry analysis. (C) Representative phase contrast (left) and FITC (right) images of PR60 CSCs firmly adhered to primary endothelial HUVECs and to brain hCMEC/D3 cells in one field of view at the end of the flow-based adhesion assay. (D), (E) Quantification of adhesion of shear-resistant PR60 CSCs cultured in vitro (D) and freshly isolated cells from PR60-IN-PDXs (E) to HUVECs and brain hCMEC/D3 cell momolayers. Firm adhesion was quantified as the number of cells per field in 10 fields of view (n/FOV) per condition (each colored black thick-bordered spot represents an individual biological replicate, and colored spots represent technical replicates; the color code identifies each biological replicate: $n = 5$ independent biological replicates in D, and $n = 3$ independent biological replicates in F). (F) Uniform Manifold Approximation and Projection (UMAP) of integrated adhered and input PR60 CSC samples, showing 12 clusters identified

known to support stemness maintenance and metastasis [40–42] (Figure 5N). Conversely, genes enriched in both non-adherent cell clusters (Figure S2F) were linked to epithelial cell differentiation (Figure S2G). Overall, these results highlight that BCBM-derived PR60 CSCs possess brain organotropism and an adhesive phenotype, two molecular and functional traits that are preserved even within the context of a primary breast cancer setting.

3.6 | PR60 CSCs are Highly Chemoresistant Cells

Despite the high genomic and transcriptomic similarity between PR60 CSCs and matching human PR60 BM (Figures 1F, 2C, and 4A), the comparison of their transcriptomes revealed an enrichment of drug resistance pathways specifically within the CSC compartment. Indeed, PR60 CSCs exhibited resistance to several drugs commonly used in BC treatment, including Tamoxifen, Aromatase inhibitors, Cisplatin, Trabectidin, and Imatinib (Figure 6A). As a functional validation approach, we screened PR60 CSCs with a drug library composed of 295 compounds, including anticancer agents and drugs effective in the central nervous system (CNS-effective drugs) (Table S3). Cells were not responsive to most of the compounds, and only 26 compounds were identified to significantly reduce cell viability (Figure 6B). A dose-response assay confirmed PR60 CSC sensitivity to the majority of these 26 agents, validating the screening results (Figure 6C). This resistant phenotype is consistent with the patient's highly aggressive clinical course, characterized by rapid deterioration following BM diagnosis and the absence of opportunity to initiate systemic therapy. Notably, although the patient had previously received Taxol in the adjuvant setting, PR60 CSCs displayed only mild sensitivity to this agent during in vitro testing (≈30% growth inhibition, Figure 6C), reflecting the treatment-refractory behavior observed clinically. A sensitivity analysis was also performed in the FR57-II and FA40 CSC samples focusing on compounds that were most effective in the PR60 model (Figure S3A, B). Importantly, only a few vulnerabilities were shared across all three models, specifically sensitivity to the anthracyclines doxorubicin and daunorubicin, while responses to other compounds varied widely. Overall, the three models displayed divergent sensitivity profiles, reflecting the expected inter-patient heterogeneity characteristic of metastatic breast cancer and underscoring the importance of evaluating multiple patient-derived CSC models to capture clinically relevant therapeutic variability. Interestingly, Tamoxifen and the aromatase inhibitor Anastrozole, both present in the compound library, showed no effect against PR60 CSCs, supporting the predicted resistance from in silico analysis. In a focused experiment with Cisplatin and Imatinib (not included in the tested library), we also measured a lack of response as hypothesized based on CSCs transcriptomic features (Figure 6D).

Given their ER+/PgR-/HER2- status (Figure 1F), we tested PR60 CSCs for sensitivity to the CDK4/6 inhibitors Abemaciclib and Palbociclib, standard therapies for ER+/HER2- metastatic BC [43, 44]. Both agents had a limited impact on PR60 CSC viability, with Abemaciclib inducing a more pronounced cell-cycle inhibitory response across the tested concentrations (Figure 6E). While this may seem discordant with clinical trial outcomes, it aligns with the known intrinsic resistance seen in about one-third of patients, who progress within 6 months of treatment [45].

These data underscore the intrinsic resistance of PR60 CSCs and their potential as a relevant preclinical model for drug testing aimed at overcoming the resistance associated with brain metastases.

4 | Discussion

In this study, we isolated CSCs from human BCBM specimens and demonstrated their potential to initiate BMs. We developed a novel preclinical model to study BCBM both in vitro and in vivo, addressing the current shortage of reliable models, which is hampering both the deciphering of the molecular basis underlying BMs and the development of novel therapeutic approaches. Despite challenges associated with the establishment of patient-derived CSC cultures, we successfully cultured CSCs from 50% of BCBM PDXs. These stem-like cells play a central role in BM pathogenesis and therapy resistance. Orthotopic injection of CSCs in mouse brains produced tumors with variable latency, likely reflecting patient-specific molecular characteristics, while maintaining the mutational and transcriptomic profiles of the original tumors, including epithelial and molecular subtypes. Of note, existing BM cell lines often largely diverge from the molecular traits of the original tumors [46]. These features make this BM avatar model of particular interest in the BM field, where the development of novel therapies is hindered by the exclusion of patients with BM from most of the clinical trials [47]. While most current BCBM models are brain-tropic clones selected through serial rounds of xenotransplantation [7], PR60 CSCs have an innate brain tropism and recapitulate the clinical progression of the patient's original tumor without requiring any in vitro/in vivo manipulation or clonal selection. Furthermore, PR60 CSCs were able to successfully colonize the brain following both ICD- and IN-injection. To our knowledge, current BCBM models able to reach the brain after IN injection are still poorly characterized, primarily due to the low incidence of spontaneous BMs [32]. Kim and colleagues described a 4T1Br4 clone that, compared to the parental 4T1 cells, displayed an increased ability to reach the brain upon mammary fat pad injection [48]. However, while 4T1Br4 cells represent a valuable syngeneic model, they do not fully replicate the heterogeneity of human tumors. Moreover, the

at 0.6 resolution in different colors. (G) UMAP embedding showing the distribution of adhered (light green) and input PR60 CSCs (dark green) across clusters. The relative proportions of the two cell populations (Input and Adhered) across the 12 clusters are reported in the bar plot (right panel). (H–K) Feature plots (top) and corresponding violin plots (bottom) are shown for the adhesion (H), stem-related (J), and differentiation (K) signatures across clusters. For the integrin signature (I), only a violin plot is shown. (L) Feature plots showing the expression CD44high/CD24low across clusters. Legend shows a color gradient of normalized expression. (M) Violin plot showing the enrichement of gene signatures associated with metastatic breast tumors in all clusters. (N) Top signaling pathways enriched in clusters with high adhesion gene expression (cluster 0, 4, 5, 11). Combined score (c) is a combination of the p-value and odds ratio calculated by multiplying the two scores as follows: c = -log(p) * oddsRatio. Feature plots (H, J, K) show signature expression by color intensity. In violin plots, the Y-axis shows expression levels, the X-axis shows clusters, and each cell is a black dot.

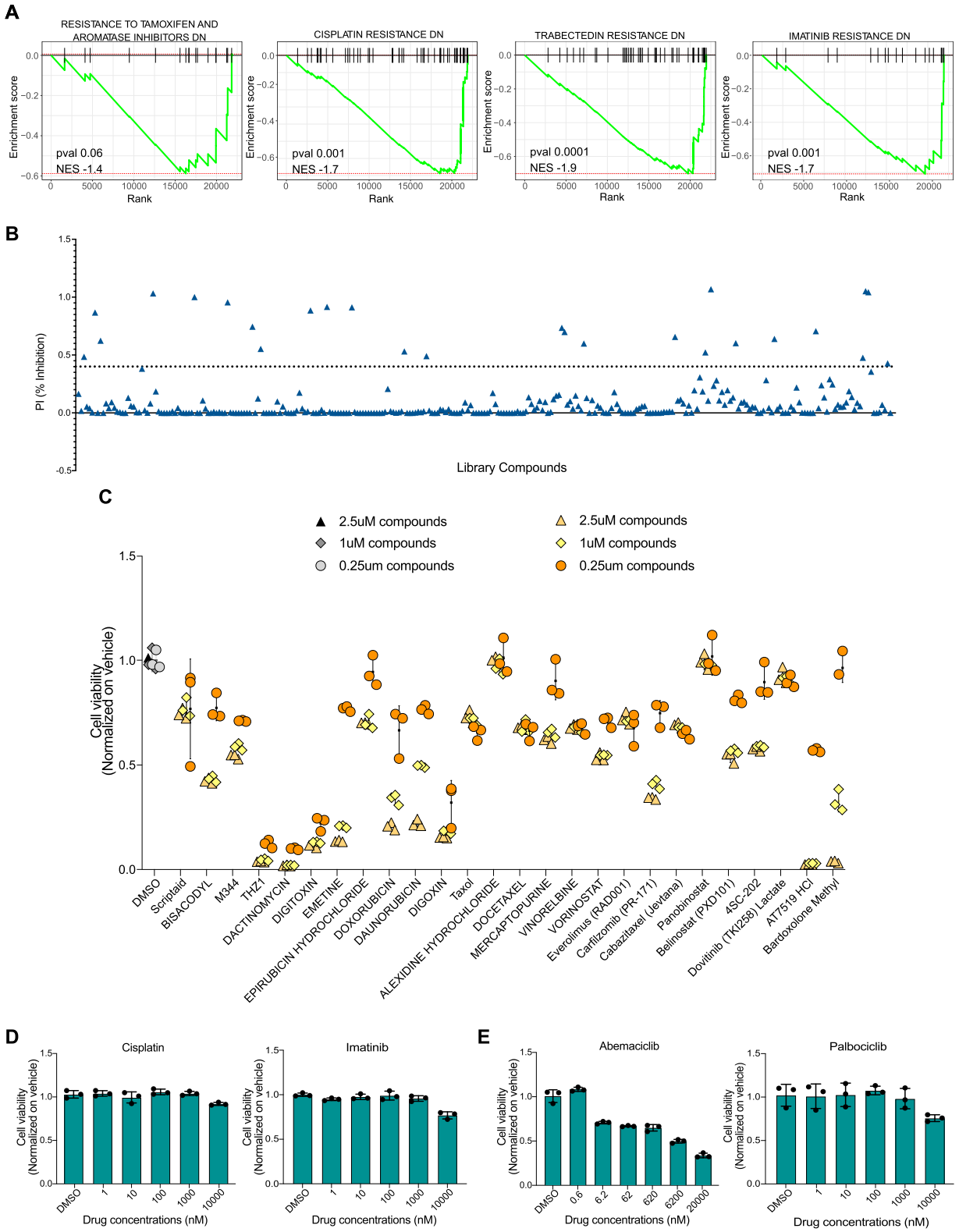

FIGURE 6 | PR60 CSCs are a relevant model for preclinal drug screening. (A) Gene Set Enrichment Analysis (GSEA) of differentially expressed genes between PR60 CSCs and metastatic brain tumors for the indicated different signatures. All signatures are enriched in PR60 CSCs. P-values and normalized enrichment scores (NES) are indicated on the plots. (B) A primary screening test with a bioactive compound library including 295 molecules was performed in PR60 CSCs. Percentage inhibition (%) has been normalized to the untreated control (0% inhibition = no drug effect). (C) A confirmation screen using the 26 candidates from the primary screen that demonstrated efficacy in targeting PR60 CSCs. (D), (E) Dose-response curves of PR60 CSCs treated with Cisplatin and Imatinib (D) or Abemaciclib and Palbociclib (E). Cell viability is expressed as a percentage relative to vehicle-treated control. Data represent mean ± SD. For the primary screening, values represent the mean of $n = 8$ technical replicates per compound concentration. Validation screening and drug sensitivity assays were performed with $n = 3$ replicates per concentration.

ability of patient-derived models to spontaneously reach the brain from mammary fat pad tumors has not yet been demonstrated [9]. PR60 CSCs represent a highly efficient model, driving BM in around 80% of mice following ICD injection, and 50% upon IN injection. This enables detailed investigation of both metastatic and premetastatic stages, providing a unique platform for the development of both therapeutic and preventive approaches.

The innate PR60 CSC organotropism for the brain is likely mediated by their preferential adhesion to brain-specific endothelial cells, as reported also in the brain-seeking clone 4T1Br4 [48]. This is in line with an earlier study describing that multiple adhesion molecules are upregulated in brain endothelial cells during micrometastatic seeding of breast cancer cells [49]. In this context, the use of BCBM-enriched CSC models in firm adhesion studies could provide valuable insights for identifying and targeting novel adhesion mediators, potentially leading to the development of preventive therapies. Moreover, we found that several adhesive molecules expressed by PR60 CSCs are intriguingly also involved in cancer stemness. Among these, CD44, Integrin $\alpha 4\beta 1$ (CD49d/CD29), VCAM-1 (CD106), and MUC1 (CD227) are known to underly the adhesion of BM circulating cells to the BBB, whereas CD227 and CD155 correlate with BC invasiveness and unfavorable prognosis, respectively [37, 38]. Moreover, the active form of Integrin $\alpha 2$ (CD49b), Integrin $\alpha 6$ (CD49f), Integrin $\beta 5$, ALCAM (CD166) are reported as enriched in different stem-like contexts [50, 51].

Additionally, single-cell analysis revealed a co-distribution of stem and adhesion markers in a subset of the bulk PR60 population, likely the MIC subpopulation. Notably, a cluster of cells depleted in the adhesion-related genes was enriched in genes associated with epithelial differentiation. These findings indicate the stem-like MICs, likely including the $CD44^{high}/CD24^{low}$ subpopulation, as primary responsible for the adhesion to brain endothelium and brain colonization.

Consistently with their stem-like nature, CSCs are adaptable entities capable of thriving in a harsh brain microenvironment and establishing pro-survival interactions with neighboring cells, including both endothelial cells and normal brain cells. PR60-derived BM express SERPINI1, which allows BM cells to both escape the pro-apoptotic signals induced by the reactive stroma and to prevent L1CAM inactivation. In turn, L1CAM expression contributes to vascular co-option, ensuring an adequate supply of oxygen and nutrients and providing a pathway along which BM cells can spread, supporting metastasis expansion [34]. The transcriptome of both orthotopic and ICD-induced tumors is shaped by the brain niche. The acquisition of Glutamate Receptor Signaling and GABA receptor signaling signatures suggests that BMs could acquire a glutamatergic or GABAergic phenotype, sustaining their proliferation by uptaking glutamate and GABA [52]. The enrichment of the Synaptogenesis Signaling Pathway and of the expression of glutamate receptors, including NMDA, AMPA, Kainate, and Metabotropic Receptors, suggests that CSCs can hijack neuronal pathways to establish neuron-to-tumor synaptic communication. Malignant synaptogenesis has been implicated in promoting glioma seeding, as well as glioma and BM proliferation and invasion [53, 54]. Notably, while gliomas are known to exploit AMPA receptor to establish both direct synapsis and perisynaptic interactions with neurons [53, 54], BMs were thought to form only pseudo-tripartite synapses through the NMDA receptor-mediated signaling [55]. However, the increased expression of AMPA receptor subunits in our experimental models suggests the need for a deeper exploration of pro-tumorigenic, bidirectional interactions between BM cells and neurons, which could open new therapeutic avenues. Although AMPA receptor inhibitors have been tested in glioma models, our data support testing these compounds in BM models as well [56]. Notably, we are also reporting the increased expression of metabotropic glutamate receptors, which have been linked to the aggressiveness of gliomas and brain-metastatic melanoma [57], potentially broadening the spectrum of therapies targeting the malignant synaptogenesis.

Due to their high genetic and transcriptomic similarity to the tumor of origin, BCBM CSCs serve as reliable models for drug testing. This, combined with their ability to recapitulate the entire metastatic cascade, provides a solid foundation for in vivo pre-clinical testing of drugs targeting both early and late stages of BM formation. Based on their transcriptomic profiles, we predicted that CSCs are highly resistant to Cisplatin, Imatinib, Tamoxifen, and Trabectidine compared to the bulk tumor of origin. Among the effective drugs, we identified Scriptaid, a pan-Histone Deacetylase inhibitor (HDACi) useful in improving the effectiveness of cisplatin in reducing metastasis and triggering glioma cell death, bisacodyl as a cytotoxic agent with selectivity for quiescent glioblastoma stem-like cells [58] and triple-negative breast cancer [59], and AT7519, an inhibitor of multiple cyclin-dependent kinases (CDKs) with high antitumor activity in preclinical models [60]. Doxorubicin, Epirubicin, and Daunorubicin exert cytotoxicity primarily through DNA intercalation and topoisomerase II inhibition, inducing double-strand breaks, apoptosis, and ROS-mediated cell death, and remain central to systemic breast cancer therapy. Taxanes (Taxol, Docetaxel, Cabazitaxel) and the vinca alkaloid Vinorelbine disrupt microtubule dynamics to cause mitotic arrest and apoptosis across breast cancer subtypes. The efficacy of these cytotoxic agents in brain metastases is largely dependent on specialized delivery strategies, such as liposomal formulations or BBB-penetrating carriers. Epigenetic modulators, including the HDAC inhibitors Vorinostat, Belinostat, Scriptaid, and 4SC-202 reprogram transcriptional networks that regulate cell cycle progression, apoptosis, epithelial–mesenchymal transition, and stemness, and modulate PI3K/AKT and receptor signaling pathways. Preclinical evidence indicates that these agents can alter metastatic phenotypes and enhance sensitivity to combination therapies, including in the context of brain colonization. Notably, the ability of the BCBM-derived CSC model to recover previously validated anticancer agents, such as those identified in the METPlatform [61], highlights its strong clinical relevance and potential as a robust tool for identifying effective therapeutic strategies against aggressive and treatment-resistant cancers.

Overall, patient-derived BCBM CSCs faithfully replicate the genetic, transcriptomic, and metastatic features of their tumors of origin and capture intratumoral heterogeneity. Our data reveal a strong link between adhesion-related and stemness-related gene expression, two features that are especially retained in the MIC subset, while non-adherent subpopulations express gene programs related to epithelial differentiation, suggesting reduced metastatic potential. These findings highlight both the clinical

relevance of BCBM CSC models as a versatile tool for both in vitro and in vivo preclinical research. Nevertheless, challenges remain in both the efficient isolation and targeting of the adhesive and stem-like MIC subset as well as in reconstructing how CSCs from primary breast tumors evolve into MICs and ultimately brain-adapted CSCs. Although matched primary–metastatic samples were unavailable in this study, reflecting a pervasive limitation in BCBM research, we find that established BCBMs contain a distinct MIC-like population that retains hallmarks of early metastatic intermediates. This suggests that the trajectory from primary CSCs to MICs to brain-resident CSCs is at least partially preserved within the metastatic lesion itself.

The lack of paired samples is a structural limitation in the field, as brain metastases often arise years after initial diagnosis and diverge extensively from their primary tumors. Nonetheless, our findings begin to reveal this trajectory and position the MIC-like subset as a key cellular state for therapeutic intervention.

Author Contributions

S.F., C.R., and D.O. contributed equally to the work as co-first authors. S.F., C.R., D.O., A.M., B.C., and M.G.F. conducted in vitro experiments; C.R., V.G., C.C., E.Z., M.G.F. performed the animal experiments; D.B.M., F.D.M. and E.M. provided human tissue samples and collected patient information; C.C. performed experiments with endothelial cells; B.W., I.A.R., and P.O.C. provided the endothelial HCMEC/D3 cells; C.M. and Z.Y. analyzed DNA data; E.C., T.G., and D.C. analyzed bulk and single-cell RNA sequencing data; G.B., M.P., B.P. and M.G.J. performed histological analysis in both human and mouse tissues; G.G. performed drug screens; S.F., C.R., D.O, M.G.F., D.T., Z.Y., D.C., S.P., G.P. contributed to data collection and interpretation; S.F., C.R., D.O., G.P. wrote the manuscript; G.P. conceived and supervised the project, and secured funding for the study. All authors read and approved the final manuscript.

Acknowledgements

The authors thank Simon Ronzoni for outstanding technical support with FACS acquisition and analysis, and the Molecular Pathology Facility for assistance with histology and immunohistochemistry. We are grateful to Alberto Dalmasso and Niccolò Roda for their support with mouse experiments. We also acknowledge the contributions of the Cell Culture and Genomics Units at the European Institute of Oncology.

Funding

This work was supported by a grant from the Italian Association for Cancer Research (AIRC, Investigator Grant ID: 27014 to G.Pelicci), and partially by the Italian Ministry of Health with Ricerca Corrente and 5 × 1000 funds (to European Institute of Oncology IRCCS).

Ethics Approval Statement

All experiments involving mice were conducted following protocols approved by the Italian Ministry of Health (Authorization no. 663/2019-PR). These protocols comply with Italian laws (D.L. vo 116/92 and subsequent amendments) and adhere to EU Directive 86/609 (Council Directive 86/609/EEC).

Consent

All patients in this study provided written informed consent for the use of their biological samples for research purposes. The study protocol was approved by the Ethics Committee of the Fondazione IRCCS Istituto Neurologico "Carlo Besta."

Conflicts of Interest

The authors declare no conflict of interest.

Data Availability Statement

Access to the NGS data by qualified researchers who wish to work with these data or validate our findings can be requested by contacting giuliana.pelicci@ieo.it.

References

1. A. S. Achrol, R. C. Rennert, C. Anders, et al., "Brain Metastases," *Nature Reviews Disease Primers* 5, no. 1 (2019): 5, https://doi.org/10.1038/s41572-018-0055-y.

2. N. U. Lin, J. R. Bellon, and E. P. Winer, "CNS Metastases in Breast Cancer," *Journal of Clinical Oncology* 22, no. 17 (2004): 3608–3617, https://doi.org/10.1200/JCO.2004.01.175.

3. H. Sun, J. Xu, S. Dai, Y. Ma, and T. Sun, "Breast Cancer Brain Metastasis: Current Evidence And Future Directions," *Cancer Medicine* 12, no. 2 (2023): 1007–1024, https://doi.org/10.1002/cam4.5021.

4. C. D. Arvanitis, G. B. Ferraro, and R. K. Jain, "The Blood–Brain Barrier And Blood–Tumour Barrier In Brain Tumours And Metastases," *Nature Reviews Cancer* 20, no. 1 (2020): 26–41, https://doi.org/10.1038/s41568-019-0205-x.

5. R. Bartsch, A. S. Berghoff, J. Furtner, et al., "Trastuzumab Deruxtecan in HER2-Positive Breast Cancer With Brain Metastases: A Single-Arm, Phase 2 Trial," *Nature Medicine* 28, no. 9 (2022): 1840–1847, https://doi.org/10.1038/s41591-022-01935-8.

6. R. K. Murthy, S. Loi, A. Okines, et al., "Tucatinib, Trastuzumab, and Capecitabine for HER2-Positive Metastatic Breast Cancer," *New England Journal of Medicine* 382, no. 7 (2020): 597–609, https://doi.org/10.1056/NEJMoa1914609.

7. M. Valiente, A. E. Van Swearingen, C. K. Anders, et al., "Brain Metastasis Cell Lines Panel: A Public Resource Of Organotropic Cell Lines," *Cancer Research* 80, no. 20 (2020): 4314–4323, https://doi.org/10.1158/0008-5472.CAN-20-0291.

8. S. Jeising, A. Nickel, J. Trübel, et al., "A Clinically Compatible In Vitro Drug-Screening Platform Identifies Therapeutic Vulnerabilities In Primary Cultures Of Brain Metastases," *Journal of Neuro-Oncology* 169, no. 3 (2024): 613–623, https://doi.org/10.1007/s11060-024-04763-7.

9. M. J. Contreras-Zárate, D. R. Ormond, A. E. Gillen, et al., "Development Of Novel Patient-Derived Xenografts From Breast Cancer Brain Metastases," *Frontiers in Oncology* 7 (2017): 252, https://doi.org/10.3389/fonc.2017.00252.

10. D. A. Lawson, N. R. Bhakta, K. Kessenbrock, et al., "Single-Cell Analysis Reveals A Stem-Cell Program In Human Metastatic Breast Cancer Cells," *Nature* 526, no. 7571 (2015): 131–135, https://doi.org/10.1038/nature15260.

11. A. S. Berghoff, Y. Liao, M. A. Karreman, et al., "Identification And Characterization Of Cancer Cells That Initiate Metastases To The Brain And Other Organs," *Molecular Cancer Research* 19, no. 4 (2021): 688–701, https://doi.org/10.1158/1541-7786.MCR-20-0863.

12. K. Ganesh, H. Basnet, Y. Kaygusuz, et al., "L1CAM Defines The Regenerative Origin Of Metastasis-Initiating Cells In Colorectal Cancer," *Nature Cancer* 1, no. 1 (2020): 28–45, https://doi.org/10.1038/s43018-019-0006-x.

13. M. Pein, J. Insua-Rodríguez, T. Hongu, et al., "Metastasis-Initiating Cells Induce And Exploit A Fibroblast Niche To Fuel Malignant Colonization Of The Lungs," *Nature Communications* 11, no. 1 (2020): 1494, https://doi.org/10.1038/s41467-020-15188-x.

14. C. M. Young, L. Beziaud, P. Dessen, A. Santamaria-Martínez, and J. Huelsken, "Metabolic Dependencies Of Metastasis-Initiating Cells In Female Breast Cancer," *Nature Communications* 14, no. 1 (2023): 7076, https://doi.org/10.1038/s41467-023-42748-8.

15. L. Seeneevassen, A. Zaafour, E. Sifré, et al., "Targeting Metastasis-Initiating Cancer Stem Cells In Gastric Cancer With Leukaemia Inhibitory Factor," *Cell Death Discovery* 10, no. 1 (2024): 120, https://doi.org/10.1038/s41420-024-01839-1.

16. G. Dontu, W. M. Abdallah, J. M. Foley, et al., "In Vitro Propagation And Transcriptional Profiling Of Human Mammary Stem/Progenitor Cells," *Genes & Development* 17, no. 10 (2003): 1253–1270, https://doi.org/10.1101/gad.1061803.

17. B. Ortensi, D. Osti, S. Pellegatta, et al., "Rai Is A New Regulator Of Neural Progenitor Migration And Glioblastoma Invasion," *Stem Cells* 30, no. 5 (2012): 817–832, https://doi.org/10.1002/stem.1056.

18. C. Cerutti and I. A. Romero, *The Blood-Brain Barrier: Methods and Protocols* (Springer, 2022), 315–331, https://doi.org/10.1007/978-1-0716-2289-6_19.

19. C. Cerutti and A. J. Ridley, "Analyzing the Roles of Rho GTPases in Cancer Cell Adhesion to Endothelial Cells Under Flow Conditions," in *Metastasis: Methods and Protocols* (Springer, 2021), 93–109, https://doi.org/10.1007/978-1-0716-1350-4_7.

20. A. Dobin, C. A. Davis, F. Schlesinger, et al., "STAR: Ultrafast Universal RNA-seq Aligner," *Bioinformatics* 29, no. 1 (2013): 15–21, https://doi.org/10.1093/bioinformatics/bts635.

21. Y. Liao, G. K. Smyth, and S. W. FeatureCounts, "Featurecounts: An Efficient General Purpose Program For Assigning Sequence Reads To Genomic Features," *Bioinformatics* 30, no. 7 (2014): 923–930, https://doi.org/10.1093/bioinformatics/btt656.

22. M. D. Robinson, D. J. McCarthy, and G. K. Smyth, "Edger: A Bioconductor Package For Differential Expression Analysis Of Digital Gene Expression Data," *Bioinformatics* 26, no. 1 (2009): 139–140, https://doi.org/10.1093/bioinformatics/btp616.

23. A. Gupta, P. Gautam, K. Wennerberg, and T. Aittokallio, "A Normalized Drug Response Metric Improves Accuracy And Consistency Of Anticancer Drug Sensitivity Quantification In Cell-Based Screening," *Communications Biology* 3, no. 1 (2020): 42, https://doi.org/10.1038/s42003-020-0765-z.

24. J. H. Zhang, T. D. Y. Chung, and K. R. Oldenburg, "A Simple Statistical Parameter For Use In Evaluation And Validation Of High Throughput Screening Assays," *SLAS Discovery* 4, no. 2 (1999): 67–73, https://doi.org/10.1177/108705719900400206.

25. R. Galli, E. Binda, U. Orfanelli, et al., "Isolation And Characterization Of Tumorigenic, Stem-Like Neural Precursors From Human Glioblastoma," *Cancer Research* 64 (2004): 7011–7021, http://aacrjournals.org/cancerres/article-pdf/64/19/7011/2518418/zch01904007011.pdf.

26. C. Li, D. G. Heidt, P. Dalerba, et al., "Identification Of Pancreatic Cancer Stem Cells," *Cancer Research* 67, no. 3 (2007): 1030–1037, https://doi.org/10.1158/0008-5472.CAN-06-2030.

27. E. Dotse and Y. Bian, "Isolation Of Colorectal Cancer Stem-Like Cells," *Cytotechnology* 68, no. 4 (2016): 609–619, https://doi.org/10.1007/s10616-014-9806-0.

28. A. Herreros-Pomares, J. D. de-Maya-Girones, S. Calabuig-Fariñas, et al., "Lung Tumorspheres Reveal Cancer Stem Cell-Like Properties And A Score With Prognostic Impact In Resected Non-Small-Cell Lung Cancer," *Cell Death & Disease* 10, no. 9 (2019): 660, https://doi.org/10.1038/s41419-019-1898-1.

29. M. R. Dionísio, A. F. Vieira, R. Carvalho, et al., "BR-BCSC Signature: The Cancer Stem Cell Profile Enriched In Brain Metastases That Predicts A Worse Prognosis In Lymph Node-Positive Breast Cancer," *Cells* 9, no. 11 (2020): 2442, https://doi.org/10.3390/cells9112442.

30. W. Xiao, S. Zheng, X. Xie, et al., "SOX_2 Promotes Brain Metastasis of Breast Cancer by Upregulating the Expression of FSCN1 and HBEGF," *Molecular Therapy—Oncolytics* 17 (2020): 118–129, https://doi.org/10.1016/j.omto.2020.03.001.

31. H. Zhou and D. Zhao, "Ultrasound Imaging-Guided Intracardiac Injection To Develop A Mouse Model Of Breast Cancer Brain Metastases Followed By Longitudinal MRI," *Journal of Visualized Experiments: JoVE* 85 (2014): 51146, https://doi.org/10.3791/51146.

32. L. Miarka and M. Valiente, "Animal Models Of Brain Metastasis," *Neuro-Oncology Advances* 3 (2021): v144–v156, https://doi.org/10.1093/noajnl/vdab115.

33. Y. Kienast, L. von Baumgarten, M. Fuhrmann, et al., "Real-Time Imaging Reveals The Single Steps Of Brain Metastasis Formation," *Nature Medicine* 16, no. 1 (2010): 116–122, https://doi.org/10.1038/nm.2072.

34. M. Valiente, A. Obenauf, X. Jin, et al., "Serpins Promote Cancer Cell Survival And Vascular Co-Option In Brain Metastasis," *Cell* 156, no. 5 (2014): 1002–1016, https://doi.org/10.1016/j.cell.2014.01.040.

35. R. R. Langley and I. J. Fidler, "Tumor Cell-Organ Microenvironment Interactions In The Pathogenesis Of Cancer Metastasis," *Endocrine Reviews* 28, no. 3 (2007): 297–321, https://doi.org/10.1210/er.2006-0027.

36. M. Klemke, T. Weschenfelder, M. H. Konstandin, and Y. Samstag, "High Affinity Interaction Of Integrin $\alpha 4\beta 1$ (VLA-4) And Vascular Cell Adhesion Molecule 1 (VCAM-1) Enhances Migration Of Human Melanoma Cells Across Activated Endothelial Cell Layers," *Journal of Cellular Physiology* 212, no. 2 (2007): 368–374, https://doi.org/10.1002/jcp.21029.

37. Y. Wang, D. Shi, Y. Liu, et al., "Aberrant Expression of CD227 Is Correlated With Tumor Characteristics And Invasiveness Of Breast Carcinoma," *Journal of Cancer Research and Clinical Oncology* 140, no. 8 (2014): 1271–1281, https://doi.org/10.1007/s00432-014-1676-5.

38. D. Zhang, J. Liu, M. Zheng, C. Meng, and J. Liao, "Prognostic And Clinicopathological Significance Of CD155 Expression In Cancer Patients: A Meta-Analysis," *World Journal of Surgical Oncology* 20 (2022): 351, https://doi.org/10.1186/s12957-022-02813-w.

39. C. Sheridan, H. Kishimoto, R. K. Fuchs, et al., "$CD44^+/CD24^-$Breast Cancer Cells Exhibit Enhanced Invasive Properties: An Early Step Necessary For Metastasis," *Breast Cancer Research* 8 (2006): R59, https://doi.org/10.1186/bcr1610.

40. P. P. Provenzano and K. P. Fred;, "The Role Of Focal Adhesion Kinase In Tumor Initiation And Progression," *Cell Adhesion & Migration* 3 (2009): 347–350, http://www.landesbioscience.com/journals/celladhesion/article/9458.

41. C. Bellomo, L. Caja, and A. Moustakas, "Transforming Growth Factor B As Regulator Of Cancer Stemness And Metastasis," *British Journal of Cancer* 115, no. 7 (2016): 761–769, https://doi.org/10.1038/bjc.2016.255.

42. F. Xie, L. Ling, H. Van Dam, F. Zhou, and L. Zhang, "TGF-β Signaling In Cancer Metastasis," *Acta Biochimica et Biophysica Sinica* 50, no. 1 (2018): 121–132, https://doi.org/10.1093/abbs/gmx123.

43. N. C. Turner, J. Ro, F. André, et al., "Palbociclib in Hormone-Receptor–Positive Advanced Breast Cancer," *New England Journal of Medicine* 373, no. 3 (2015): 209–219, https://doi.org/10.1056/nejmoa1505270.

44. G. W. Sledge, M. Toi, P. Neven, et al., "MONARCH 2: Abemaciclib in Combination With Fulvestrant in Women With HR^+/HER^{2-} Advanced Breast Cancer Who Had Progressed While Receiving Endocrine Therapy," *Journal of Clinical Oncology* 35 (2017): 2875–2884, https://doi.org/10.1200/JCO.

45. E. S. Knudsen, G. I. Shapiro, and K. Keyomarsi, "Selective CDK4/6 Inhibitors: Biologic Outcomes, Determinants Of Sensitivity, Mechanisms Of Resistance, Combinatorial Approaches, And Pharmacodynamic Biomarkers," *American Society of Clinical Oncology Educational Book* 40 (2020): 115–126, https://doi.org/10.1200/edbk_281085.

46. K. Liu, P. A. Newbury, B. S. Glicksberg, et al., "Evaluating Cell Lines As Models For Metastatic Breast Cancer Through Integrative Analysis Of Genomic Data," *Nature Communications* 10, no. 1 (2019): 2138, https://doi.org/10.1038/s41467-019-10148-6.

47. R. R. Patel, V. Verma, A. B. Miller, et al., "Exclusion Of Patients With Brain Metastases From Cancer Clinical Trials," *Neuro-oncology* 22 (2020): 577–579, https://doi.org/10.1093/neuonc/noz246.

48. S. H. Kim, R. P. Redvers, L. H. Chi, et al., "Identification Of Brain Metastasis Genes And Therapeutic Evaluation Of Histone Deacetylase Inhibitors In A Clinically Relevant Model Of Breast Cancer Brain Metastasis," *DMM Disease Models and Mechanisms* 11, no. 7 (2018): DMM034850, https://doi.org/10.1242/dmm.034850.

49. M. S. Soto, S. Serres, D. C. Anthony, and N. R. Sibson, "Functional Role Of Endothelial Adhesion Molecules In The Early Stages Of Brain Metastasis," *Neuro-Oncology* 16, no. 4 (2014): 540–551, https://doi.org/10.1093/neuonc/not222.

50. V. Adorno-Cruz, A. D. Hoffmann, X. Liu, et al., "ITGA2 Promotes Expression of ACLY and CCND1 In Enhancing Breast Cancer Stemness And Metastasis," *Genes & Diseases* 8, no. 4 (2021): 493–508, https://doi.org/10.1016/j.gendis.2020.01.015.

51. A. Bianchi-Smiraglia, S. Paesante, and A. V. Bakin, "Integrin β5 Contributes to the Tumorigenic Potential Of Breast Cancer Cells Through The Src-FAK and MEK-ERK Signaling Pathways," *Oncogene* 32, no. 25 (2013): 3049–3058, https://doi.org/10.1038/onc.2012.320.

52. J. Neman, J. Termini, S. Wilczynski, et al., "Human Breast Cancer Metastases To The Brain Display GABAergic Properties In The Neural Niche," *Proceedings of the National Academy of Sciences* 111, no. 3 (2014): 984–989, https://doi.org/10.1073/pnas.1322098111.

53. H. S. Venkatesh, W. Morishita, A. C. Geraghty, et al., "Electrical And Synaptic Integration Of Glioma Into Neural Circuits," *Nature* 573, no. 7775 (2019): 539–545, https://doi.org/10.1038/s41586-019-1563-y.

54. V. Venkataramani, D. I. Tanev, C. Strahle, et al., "Glutamatergic Synaptic Input To Glioma Cells Drives Brain Tumour Progression," *Nature* 573, no. 7775 (2019): 532–538, https://doi.org/10.1038/s41586-019-1564-x.

55. Q. Zeng, I. P. Michael, P. Zhang, et al., "Synaptic Proximity Enables NMDAR Signalling To Promote Brain Metastasis," *Nature* 573, no. 7775 (2019): 526–531, https://doi.org/10.1038/s41586-019-1576-6.

56. J. Dalmau, T. Armangué, J. Planagumà, et al., "An Update On Anti-NMDA Receptor Encephalitis For Neurologists And Psychiatrists: Mechanisms And Models," *The Lancet Neurology* 18, no. 11 (2019): 1045–1057, https://doi.org/10.1016/S1474-4422(19)30244-3.

57. J. Mondal and J. T. Huse, "Neurotransmitter Power Plays: The Synaptic Communication Nexus Shaping Brain Cancer," *Acta Neuropathologica Communications* 13, no. 1 (2025): 85, https://doi.org/10.1186/s40478-025-02009-9.

58. J. Dong, F. J. Aulestia, S. A. Kahn, et al., "Bisacodyl and Its Cytotoxic Activity On Human Glioblastoma Stem-Like Cells Implication of Inositol 1,4,5-triphosphate Receptor Dependent Calcium Signaling," *Biochimica et Biophysica Acta (BBA)—Molecular Cell Research* 1864, no. 6 (2017): 1018–1027, https://doi.org/10.1016/j.bbamcr.2017.01.010.

59. W. C. Reinhold, E. Marangoni, F. Elloumi, et al., "Acetalax and Bisacodyl for the Treatment of Triple-Negative Breast Cancer: A Combined Molecular and Preclinical Study," *Cancer Research Communications* 5, no. 2 (2025): 375–388, https://doi.org/10.1158/2767-9764.CRC-24-0435.

60. D. Mahadevan, R. Plummer, M. Squires, et al., "A Phase I Pharmacokinetic and Pharmacodynamic Study of AT7519, A Cyclin-Dependent Kinase Inhibitor In Patients With Refractory Solid Tumors," *Annals of Oncology* 22, no. 9 (2011): 2137–2143, https://doi.org/10.1093/annonc/mdq734.

61. L. Zhu, D. Retana, P. García-Gómez, et al., "A Clinically Compatible Drug-Screening Platform Based On Organotypic Cultures Identifies Vulnerabilities To Prevent And Treat Brain Metastasis," *EMBO Molecular Medicine* 14, no. 3 (2022): EMMM202114552, https://doi.org/10.15252/emmm.202114552.

Supporting Information

Additional supporting information can be found online in the Supporting Information section.

Supporting File 1: adhm71020-sup-0001-SuppMat.docx.

Supporting File 2: adhm71020-sup-0002-Video S1.m4v.

Supporting File 3: adhm71020-sup-0003-Video S2.m4.v